National Aeronautics and Space Administration

Orbital Debris Quarterly News

Volume 22, Issue 4
November 2018

Inside...

A publication of the NASA Orbital Debris Program Office

A SOZ Unit Breaks Up in August 2018

For the second calendar quarter in a row, a SOZ (*Sistema Obespecheniya Zapuska*) ullage motor or SL-12 auxiliary motor, from a Proton Block DM fourth stage, has broken up. The SOZ fragmented at 21:59Z on 24 August 2018 after approximately 12.67 years on-orbit. These motors have a long history of fragmentations, this event being the 49th breakup of this class of object over its program history. A total of 380 SL-12 Auxiliary Motors were cataloged between 1970 and 2012, of which 64 remain on orbit as of 10 October 2018. Of these 64, 35 are now believed to be intact. The remaining 29 have fragmented and remain on-orbit while an additional 20 fragmented parent bodies have reentered.

Ullage motors, used to provide three-axis control to the Block DM during coast and to settle propellants prior to an engine restart, were routinely ejected after the Block DM stage ignites for the final time.

This SOZ unit (International Designator 2005-050F, U.S. Strategic Command [USSTRATCOM] Space Surveillance Network [SSN] catalog number 28920) is associated with the launch of the Cosmos 2417-2419 spacecraft, members of the Russian global positioning navigation system (GLONASS) constellation.

The motor was in a highly elliptical 18949 x 546 km orbit at an inclination of 65.3° at the time of the breakup; the event is estimated to have occurred at an altitude of approximately 4090.1 km at a latitude of 41.6° North and longitude of 236.9° East. Approximately 20 pieces have been observed, but due to difficulties in tracking objects in deep space elliptical orbits, this event may have produced many more fragmentation debris than have been observed to date. The nature of these objects was identified by Dr. Boris V. Cherniatiey, Deputy Constructor for the Energiya NPO, who had previously served as Chief Constructor for the Block DM stage in October 1992 [1]. It is assumed that the cause of this fragmentation is related to the residual hypergolic propellants on board and failure of the membrane separating the fuel and oxidizer.

Reference

1. Chernyavskiy, G.M, Johnson, N.L., and McKnight, D.S. "Identification and Resolution of an Orbital Debris Problem with the Proton Launch Vehicle," Proceedings of the First European Conference on Space Debris, ESA SD-01, pp. 575-580, (July 1993). ♦

Atlas V Upper Stage Fragmentation Event Concludes an Active August 2018

The third fragmentation event of August occurred 31 August with the breakup of a U.S. upper stage rocket booster. The upper stage booster fragmented at approximately 02:00Z on 31 August 2018 after approximately 3.96 years on-orbit. This Centaur (International Designator 2014-055B, U.S. Strategic Command [USSTRATCOM] Space Surveillance Network [SSN] catalog number 40209) is associated with the launch of the USA 257 spacecraft. Based on the information provided by the Combined Space Operations Center via the space-track website, approximately 70 associated fragments are being tracked and incorporated into routine conjunction assessment process. There is no indication that the breakup was caused by a collision. ♦

PROJECT REVIEW

Implication of Debris Fragment Shape on Shield Protection Capability

J.E. MILLER

The DebriSat hypervelocity impact experiment was performed at the Arnold Engineering Development Center on 15 April 2014 (ODQN, Vol. 18, Issue 3, pp. 3-5). Its intended use is to update the catastrophic break-up models for satellites of modern construction [1]. To this end, the DebriSat was built with modern materials including structural panels of carbon-fiber reinforced polymer (CFRP). Subsequent to the experiment, fragments of the DebriSat have been extracted from porous soft-catch panels that were used to gather the debris from the impact event [2]. Thus far, one of the key observations from the collected fragments is that CFRP fragments represent a large fraction of the collected debris and that these fragments tend to be thin, flake-like structures or long, needle-like structures; whereas, debris with nearly equal dimensions is less prevalent. As current ballistic-limit models for shields are all based upon spherical impacting particles [3], the experiment has pointed to a missing component in the current approach to ballistic modeling that must be considered.

While numerous shield types are currently in use for impact protection from orbital debris and meteoroids, a common shield in use is the double-wall shield referred to frequently as a Whipple shield [4]. This shield achieves a high level of ballistic performance for minimal weight because the stresses induced in a projectile during impact are far above the stresses the solid particle can withstand, resulting in a break-up of the particle. In the double-wall approach, an empty volume between the two walls of the shield gives a space for the debris to expand, resulting in a distributed impact on the second shield-wall. Even with the increased performance of this design, the shield-wall reaches a limit, which is the ballistic-limit of the shield-system [3]. Commonly, the ballistic-limit is characterized through experiment to a characteristic dimension of the projectile, which has largely been based on the diameter of a sphere [3].

Spheres have beneficial qualities for shield characterization as there is no angle-of-attack dependence for the shape (*i.e.*, a sphere looks the same regardless of the orientation of the projectile on impact). Spheres also have some ballistic benefits as they result in a relatively uniform stress-state across the projectile [5]. Furthermore, the shock waves originating from the sphere push material in the first wall approximately radially, which improves the spread of material [5]. It has been experimentally observed with aluminum particles that departing from a spherical shape has a consequence for all-aluminum, double-wall shield performance, at least, for particles impacting normal to the surface [6-8].

Complicating these experimental observations is that the pure, all-metal, Whipple shield is less prevalent in deployment due to thermal challenges with the shield. The presence of thermal shielding materials is known to affect the performance of double-wall shields depending on the construction and the placement of the thermal blanket, thus thermal materials should be included in an analysis to be representative of actual spaceflight [3]. NASA and other agencies have performed numerous experimental campaigns on flight configurations with thermal materials, and among those, a Whipple shield with a thermal blanket attached to the front of the outer bumper has been selected for this numerical study [9]. This shield has the material configuration shown in Fig. 1.

At the core of the shield is an aluminum, double-wall configuration, but external to it is a multi-layer blanket with fabrics and metals that create an intermediate separation of the materials. This shield is typical of ISS shields with the smallest critical particles resulting in penetration by orbital debris and meteoroids. Due to the lower

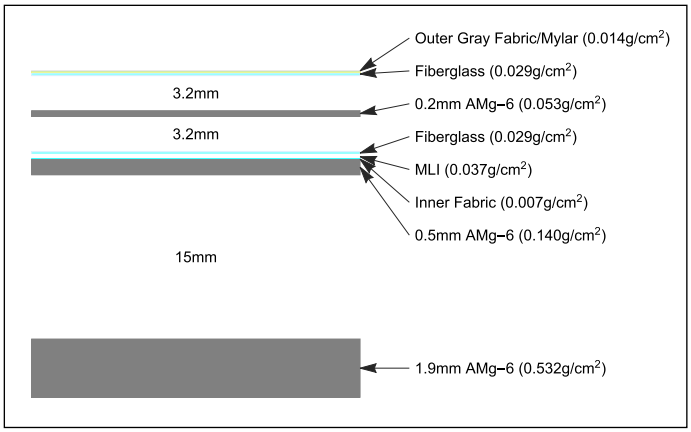

Figure 1. Shield numerical simulation configuration schematic (layers scaled by mass; separations to scale).

continued on page 3

Debris Fragment Shape

continued from page 2

capability, these shields have been selected for this study as the most sensitive to penetration by the observed CFRP fragments from the DebriSat experiment.

The simulations of this numerical study are similar to those described by Carrasquilla and Miller [10] where metallic, ellipsoidal projectiles impacting an all-aluminum, double-wall shield were considered. Similar to Ref. 10, these simulations have been performed using the multi-dimensional, nonlinear, structural-dynamics suite of codes called CTH [11]. The simulations use a three-dimensional, rectangular mesh with a minimum cubic cell-size of 0.15 mm in the vicinity of the impact. All together the simulation space extends to a minimum of 6 cm from the impact location. In time, the simulations are performed to at least 35 μs elapsed time after impact. If structural elements continue to evolve in time-lapsed evaluation, simulations are extended until the movement is less than a meter per second.

An illustration of a pair of representative simulations is shown in Fig 2. In this graphic, logarithmic density contours of the mid-plane of the simulation space are shown. The density contours range over five decades from 10^{-4} g/cm^3 to 10 g/cm^3; although, in the simulations the material is tracked until 10^{-5} g/cm^3. In Fig. 2a the simulation of an impact of a right-circular cylinder with a diameter of 8.8 mm and length of 0.275 mm (L/D ratio of 1:32) is shown. For this impact simulation, the central-axis of the cylinder is aligned with the velocity vector for a 7 km/s impact into the surface-normal of the shield. In Fig. 2b, this graphic shows a simulation of an equivalent impact condition and diameter, but in this simulation the length of the right-circular cylinder is 0.55 mm (*i.e.*, twice as long and as massive, an L/D of 1:16).

The upper contours in both Fig. 2a and 2b are the density distributions immediately prior to impact. Moving from top to bottom is the projectile and then the blanket, as described in Fig. 1, then the aluminum, double-wall shield. The lower contours are the density distribution in the same plane after 35 μs of material motion from the impact. As can be seen in the lower contours, the projectile has created a hole in the blanket and outer-wall materials, and impact remnants have expanded to a low-density vapor within the volume between the walls. Comparing the rear walls in Fig. 2a to Fig. 2b, it can be seen that the shield can withstand an 8.8 mm-diameter, right-circular cylinder that is 0.275 mm long at 7 km/s, but the 0.55 mm-long cylinder at the same speed defeats the shield. The collection of these two simulations identifies the critical length for the shield, which is 0.41±0.14 mm. This same approach has been performed for a broad collection of diameters of cylinders, as indicated in Fig. 3.

In Fig. 3a, the simulated lengths of right-circular cylinders with the cylinder-axis aligned with the velocity vector and the shield surface-normal vector are shown for cylinder diameters ranging from 0.275 mm to 13.2 mm. In this figure, the lengths that did not result in a penetration, like Fig. 3a, are shown as open circles, and the lengths that did result in a penetration are shown as filled circles. These two lengths identify the critical length as a function of cylinder diameter for a cylinder impacting at 7 km/s normal to the shield surface, which can be seen to plateau at small diameters near 6 mm then decrease to another plateau at less than 0.5 mm for large diameters.

As noted before, a cylinder does not look the same if it impacts at an attack-angle relative to its velocity vector as illustrated in Fig. 3. Similar simulations have been performed with the cylinders' central-axis rotated 45° and 90° to the velocity vector as shown in Figs. 3b and 3c, respectively. Like before, the lengths that do not penetrate the rear wall of the shield are left open, and the lengths that do penetrate the rear wall are filled. Comparing the three figures side-by-side, it can be seen that while the 0° case can reach a length that no cylinder fails the shield, there are cases where large-diameter short-cylinders (coin-like shapes) will penetrate the shield if the orientation is with the edge impacting into the shield. Similarly, when the diameter of the cylinder is very small, impacts rotated away from aligned can have critical lengths that are very long. Finally, when the cylinder is aligned with the velocity vector, a maximum, critical length is achieved that is very similar to the maximum allowable diameter at about 6 mm for the case illustrated in Fig. 3c.

Table 1 gives a summary of some of the

continued on page 4

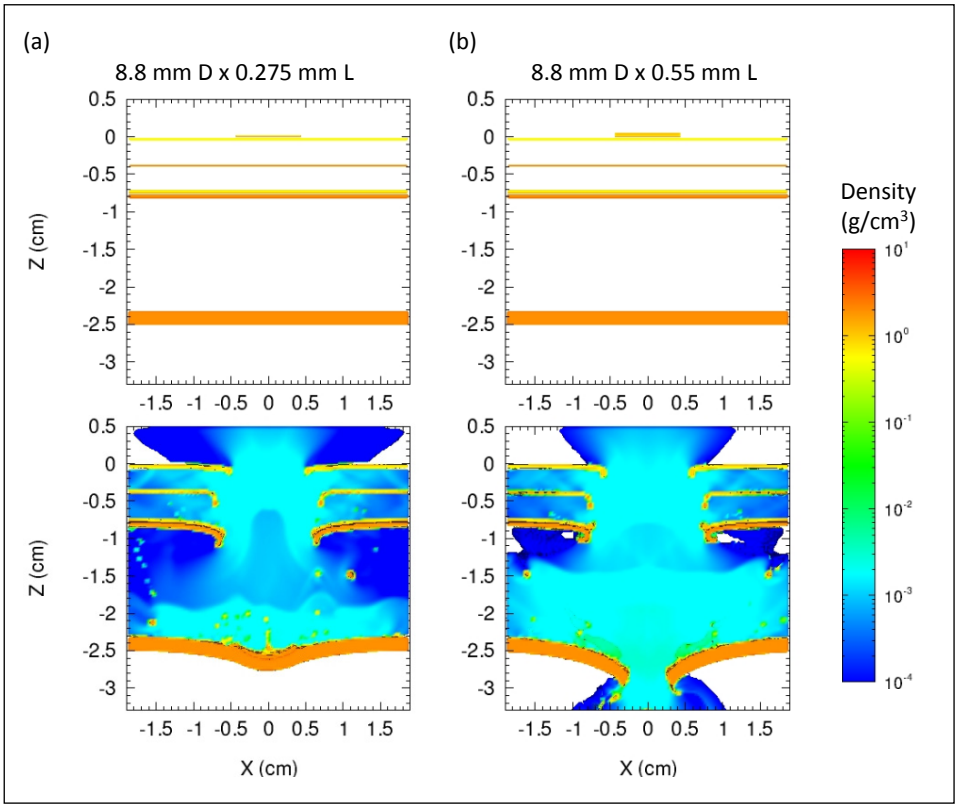

Figure 2. Density contour plots over 5 decades from 10 g/cm^3 to 10^{-4} g/cm^3 for simulations of 8.8 mm-diameter, right-circular cylindrical CFRP projectiles of length a) 0.275 mm and b) 0.55 mm. The simulated impact is with the cylindrical axis aligned to the velocity vector and surface-normal of the shield. The speed of the projectile is 7 km/s. The contours show the density contours the instant before impact (upper graphic) and after 35 μs (lower graphic). The critical impact length for this simulated condition is about 0.41 mm, as demonstrated by the intact rear wall for the cylinder length of 0.275 mm and the perforated rear wall for the cylinder length of 0.55 mm.

Debris Fragment Shape

continued from page 3

keyfindings for the assessed shield for cylinders and spheres. The cylinders of Table 1 either have a length or a diameter of 1 mm.

In all, it requires almost 50 simulations to characterize a shield to the level that has been outlined here for this single impact condition of material, speed, and obliquity. For more refined results, adding additional projectile attack-angles beyond the three that have been considered would increase this requirement further. Future simulation work is underway to expand on impact speed and obliquity of the cylindrical projectiles into the subject shield, along with other shields. In addition to the simulation efforts, hypervelocity impact experiments also are in progress to develop the means to validate simulations for the variety of projectile shapes that will be evaluated.

Table 1. CFRP projectile shape, size and mass on failure threshold of the shield studied, impacting at 7 km/s and normal to the shield surface.

Projectile Shape	Length/Diameter (L/D)	Projectile Size (mm)	Projectile Mass (g)	Impact Orientation
Sphere	-	4.3D	0.061	N/A
Needle-like cylinder	(L/D = 6.1:1)	1.0Dx6.1L	0.070	Cylinder-axis aligned with the velocity vector
Flake-like cylinder	(L/D = 1:5.3)	5.3Dx1.0L	0.039	Cylinder-axis orthogonal to the velocity vector
Flake-like cylinder	(L/D = 1:5.8)	5.8Dx1.0L	0.056	Cylinder-axis aligned with the velocity vector

References

1. Liou, J.-C., *et al*. "DebriSat-A planned laboratory-based satellite impact experiment for breakup fragment characterization," International Astronautic Congress Proceedings, IAC-16. A6.2.8x35593, (2016).

2. Fitz-Coy, N., *et al*. "Characterization of debris from the DebriSat hypervelocity test," 66th International Astronautical Congress at Jerusalem, Israel, IAC-15-A6.2.9x30343, pp. 1-10, (2015).

3. Christiansen, E.L. "Meteoroid/debris shielding," NASA/TP-2003-210788, (2003).

4. Whipple, F.L. "Meteorites and space travel," *Astronomical Journal*, 52:1161, 131, (1947).

5. Miller, J.E., Bjorkman, M.D., Christiansen, E.L., and Ryan, S.J. "Analytic ballistic performance model of Whipple shields," *Procedia Engineering*, 103, pp. 389-397, (2015).

6. Christiansen, E.L. and Kerr, J.H. "Projectile shape effects on shielding performance at 7 km/s and 11 km/s," *International Journal of Impact Engineering*, 20:1-5, pp. 165-172, (1997).

7. Piekutowski, A.J. "Hypervelocity impact of non-spherical projectiles: observations and lessons learned from impact tests," Proceedings of the Hypervelocity Shielding Workshop, ed. H. Fair, Institute of Advanced Technology: Texas, (1998).

8. Schafer, F. Hiermaier, S. and Schneider, E. "Ballistic-limit equation for the normal impact of unyawed ellipsoid-shaped projectiles on aluminium Whipple shields," 54th International Astronautical Congress at Bremen, Germany, IAC-03-IAA.5.3.06, pp. 1-10, (2003).

9. Davis, B.A. "NASA NESC high-velocity impact (HVI) study at UDRI: Phase-1," NASA Johnson Space Center report 66578, (2013).

10. Carrasquilla, M.J. and Miller, J.E. "Shape effect analysis of aluminum projectile impact on Whipple shields," *Procedia Engineering*, 204, pp. 308-314, (2017).

11. McGlaun, J., *et al*. "CTH: a three-dimensional shock wave physics code," *International Journal of Impact Engineering*, 10, pp. 351-360, (1990). ♦

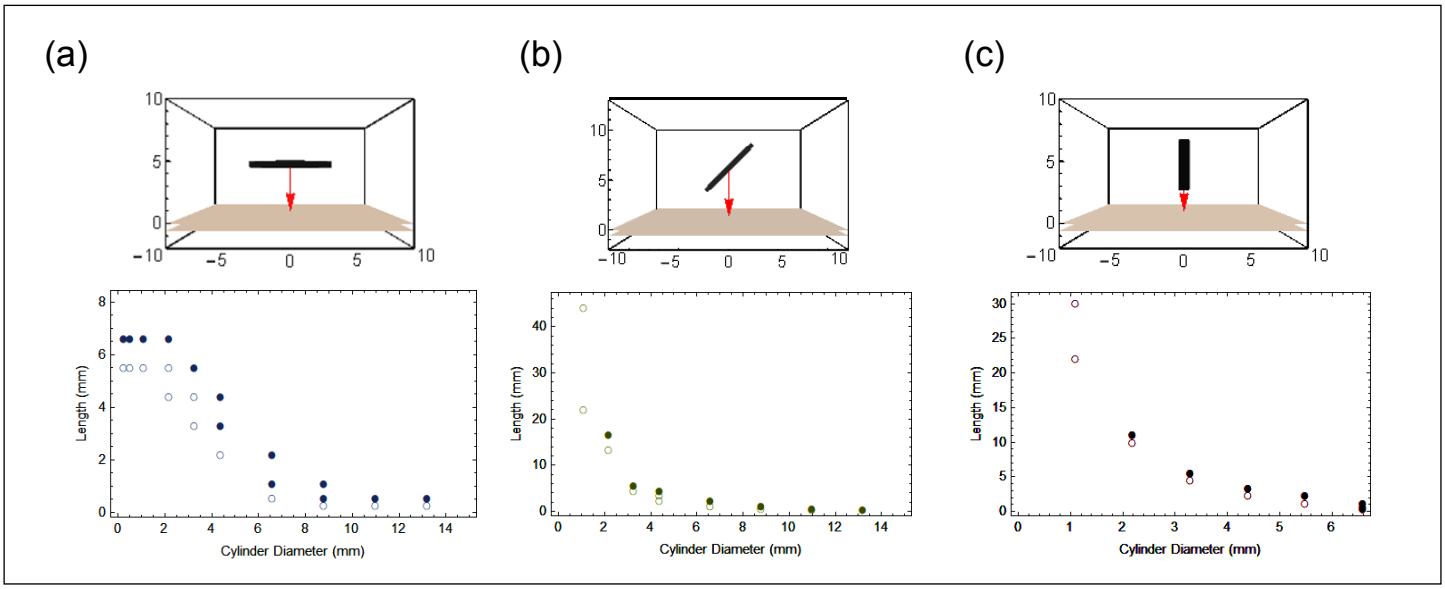

Figure 3. Collection of the simulated shield performance for ranges of cylinder diameters when the cylinder's cylinder-axis is a) aligned with the velocity vector, b) rotated 45° from the velocity vector, and c) rotated 90° from the velocity vector. Each of the three impact orientations are illustrated above the cylinder length versus cylinder diameter plots. In the plots, open circles indicate a cylinder length where the shield defeated the projectile, and filled cylinders indicate a cylinder length where the shield is defeated.

Update to the Ground Population Model in DAS 3.0

C. OSTROM

Computing ground casualty risk due to reentering spacecraft requires an accurate estimate of the human population as well as its distribution over the Earth's surface. The model included in DAS 2.1.1, (released 18 January 2017), for assessment of NASA Standard 8719.14 (NASA-STD) Requirement 4.7-1 "Casualty Risk from Reentry Debris" was developed by Opiela and Matney, based on U.S. Census Bureau International Data Base (IDB) and United Nations World Population Prospects (WPP) projections for the years 2010-2070, as well as the Gridded Population of the World, version 2 (GPWv2) dataset [1-4]. The GPWv2 dataset consists of population counts in grid cells that cover the surface of the Earth from approximately 85 degrees north latitude to 60 degrees south latitude; each grid cell covers 2.5 arcminutes of latitude by 2.5 arcminutes of longitude, approximately 4.5 km square at the equator (Fig. 1, reproduced from [1]).

The gridded population counts were separated by country or area then projected forward using the IDB figures for 2010-2050 and the global WPP figures for 2051-2070. For uncontrolled reentries in the far future, we do not expect a 'preferred' reentry longitude, so we choose to eliminate longitude variation by summing populations along each latitude band, arriving at a distribution of population only as a function of latitude, for a given year (Fig. 2).

A reentering space object does not affect the entire population of the world but only those that live under its possible ground tracks, governed by its orbital inclination. Opiela and Matney propose a weighting function based on an idealized orbit that accounts for the longer dwell time around the boreapsis and notoapsis, the northernmost and southernmost points in an orbit, respectively [1]. The latitudinal population distribution is multiplied by this weighting function to arrive at an inclination-dependent, latitude-averaged population density. We then have a single value for sub-satellite population density for each inclination (in increments of 0.1°) and reentry year (Fig. 3).

For DAS 3.0, we have updated the IDB and WPP projections to their 2017 published versions, and improved the grid resolution by using the latest Gridded Population of the World, version 4 (GPWv4) dataset (now featuring 30-arcsecond-square grid cells). The higher-resolution GPWv4 results in a noisier distribution of population as a function (see Fig. 4) when compared with the previous model. Ostrom computed the ground populations using the same procedure, while also accounting for the effects of Earth's oblateness (Fig. 5) [5]. Finally, the new inclination-dependent, latitude-averaged population density model was built using the new data, and compared with the previous GPWv2 projection for 2010.

With the inclination-dependent, latitude-averaged population density computed for each year from 2010-2100 and for all inclinations, in increments of 0.1°, DAS can estimate risk due to uncontrolled reentry of a user-defined satellite. The number of satellite fragments that survive reentry to impact the ground is determined by running the ORSAT-Derived Destructive Entry Routines (ODDER), either through the Requirement 4.7-1 assessment, or through the Reentry Survivability Analysis utility. ODDER then computes the debris casualty area (DCA) using equation 4.7-1 in NASA-STD (Eq. 1), where 0.6 is the square root of the average area of a human, and A_i is the area of an impacting fragment with greater than 15 J of kinetic energy [6]. Requirement 4.7-1

continued on page 6

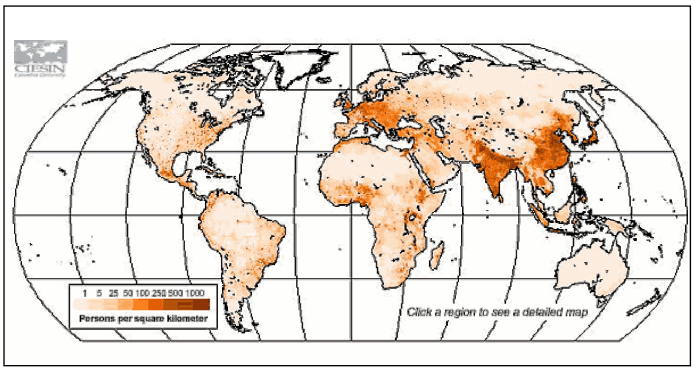

Figure 1. Global population density, 1995 (United Nations adjusted, Robinson Projection).

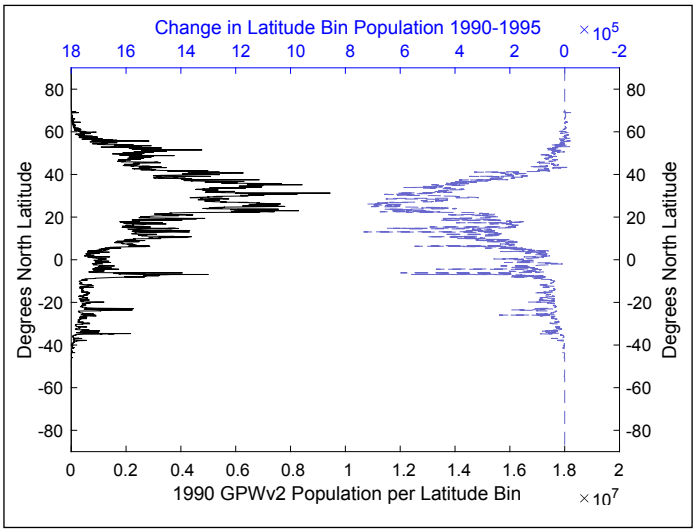

Figure 2. 1990 GPWv2 latitudinal population variation and the change in population distribution between 1990 and 1995.

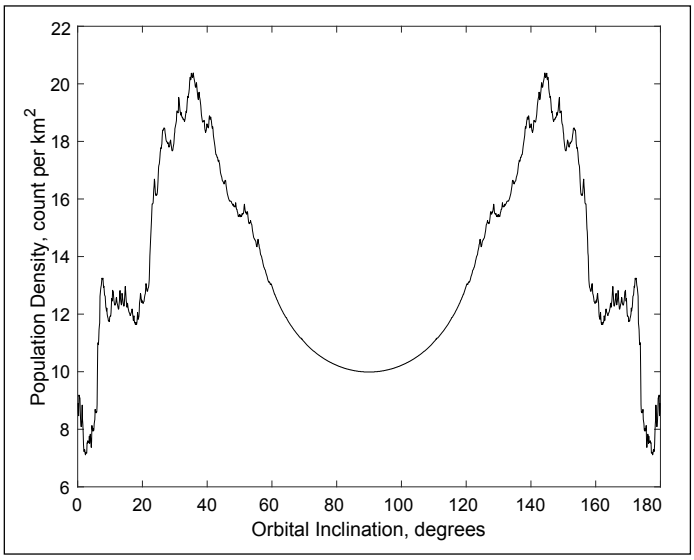

Figure 3. Variation of inclination-dependent, latitude-averaged population density with orbital inclination for 2010 based on GPWv2 and 2002 IDB andWPP data.

Ground Population Model

continued from page 5

of NASA-STD states that the risk of human casualty due to any uncontrolled reentry shall not exceed 1:10,000; this risk is calculated using the DCA from Eq. 1 and equation 4.7-2 from NASA-STD (Eq. 2), where P_D is the inclination-dependent, latitude-averaged population density.

$$DCA = \sum_{i=1}^{N} \left(0.6 + \sqrt{A_i}\right)^2 \qquad \text{(Eq. 1)}$$

$$E_C = DCA * P_D \qquad \text{(Eq. 2)}$$

The difference between the global population predicted by DAS 2.1.1 (via IDB and WPP projections and GPWv2 distribution) and the DAS 3.0 (via 2017 IDB and WPP projections and GPWv4 distribution) differs by less than 0.08% in the year 2010. However, the higher-resolution population grid provided by GPWv4 indicates that the population growth has not occurred equally at all latitudes, so some inclinations have seen sub-satellite population density increases of up to 25% over the previous prediction (others have seen decreases of up to 6%; median change is an increase of 1.2%; average change is an increase of 1.7%). As a result, the calculated risk is higher for the same mission than previously estimated (Table 1).

Table 1. Percent change in inclination-dependent, latitude-averaged population density from DAS 2.1.1 to DAS 3.0, for 2040 and 2070 reentry example cases.

	28.5°-Inclination	51.6°-Inclination	98.14°-Inclination
2040 Reentry	7.4%	4.1%	5.1%
2070 Reentry	7.0%	2.3%	4.6%

References

1. Opiela, J., and Matney, M. "Improvements to NASA's Estimation of Ground Casualties from Reentering Space Debris," IAA 03-5.4.03, 54th International Astronautical Congress of the International Astronautical Federation, the International Academy of Astronautics and the International Institute of Space Law, Bremen, Germany, October 2003.

2. United States Bureau of the Census, "International Data Base." Available at: https://www.census.gov/data-tools/demo/idb/informationGateway.php, accessed 16 June 2017.

3. United Nations. "World Population Prospects 2017," Available at https://population.un.org/wpp/, accessed 16 June 2017.

4. Center for International Earth Science Information Network (CIESIN). "Gridded Population of the World (GPW), Version 2," Columbia University, International Food Policy Research Institute (IFPRI) and World Resources Institute (WRI), Palisades, NY, (2000).

5. Ostrom, C. "Improving Estimation of Ground Casualty Risk from Reentering Space Objects", 9th International Association for the Advancement of Space Safety Conference, Toulouse, France, (October 2017).

6. National Aeronautics and Space Administration. "Process for Limiting Orbital Debris," NASA-STD-8719.14A (with Change 1), approved 2011-12-08. ♦

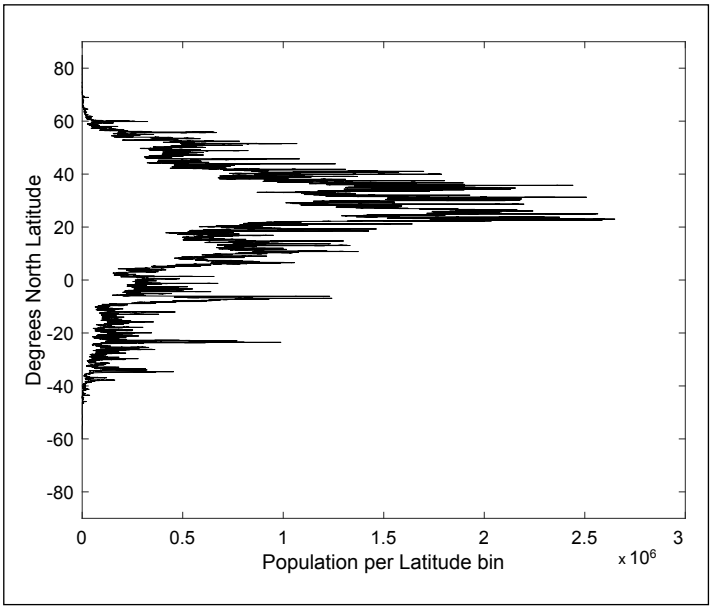

Figure 4. 2010 GPWv4 latitudinal population variation.

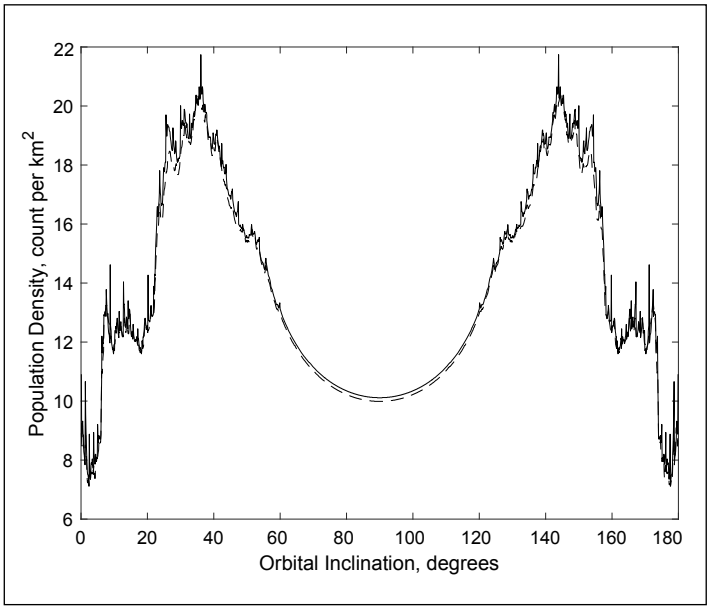

Figure 5. Comparison of GPWv2 densities on a spherical Earth (dashed line), and GPWv4 densities on an ellipsoidal Earth (solid line) for reentries in 2010, as a function of orbital inclination.

CONFERENCE REPORTS

The 19th Advanced Maui Optical and Space Surveillance Technologies Conference (AMOS), 11-14 September 2018, Maui, Hawaii, USA

The 19th Advanced Maui Optical and Space Surveillance Technologies Conference was held 11-14 September. This year AMOS broke the record with 840 participants, including 118 representing international partners from 23 countries. The opening keynote speaker was Major General Stephen N. Whiting from U.S. Strategic Command and Air Force Space Command. Maj. General Whiting discussed the reorganization within the Air Force Space Command and focused on various areas, both military and non-military, of Space Situational Awareness (SSA), preserving peace in the space domain, and the additional stresses on SSA from large constellations.

The keynote addresses were given by 1) Kevin O'Connell, Director of the Office of Space Commerce and U.S. Department of Commerce, 2) Sei-Joong Kwon, Director of Climate Change, Energy, Environment and Scientific Affairs, as well as the ministry of Foreign Affairs representing the Republic of Korea, and 3) Richard Buenneke, Senior Advisor for the National Security Space Policy at the U.S. Department of State.

Six papers were presented during the Orbital Debris Session; James Frith, from the NASA Orbital Debris Program Office (ODPO) was the session co-chair. The first session speaker, Aaron J. Rosengren (University of Arizona), explored using orbital resonances caused by lunisolar perturbations for passive orbital debris removal. Benjamin Bastida Virgili (ESA/ESOC Space Debris Office) presented work on the effectiveness of combining multiple data sources to improve timing and location re-entry predictions. He was followed by Emilano Cordelli (Astronomisches Institut Universität Bern), who spoke about his work collecting simultaneous multi-filter observations of various space debris objects. Next, Gouri Radhakrishnan (The Aerospace Corporation) outlined the use and possible advantages of using laser ablation to simulate how materials are affected during hyper-velocity impacts. Weston Faber (L3 Applied Defense Solutions) spoke about determining the blast point for detected breakup events. Finally, Zachary Slatton (Air Force Space Command) described the methods used by the 18th Space Control Squadron to characterize detected GEO breakup events.

The Non-Resolved Optical Characterization Session, co-chaired by Heather Cowardin (NASA ODPO), focused on remote photoacoustic signatures, vibrometry challenges in measuring faraway objects in orbit, space object classification via deep convolutional neural networks, attitude detection of a CubeSat using experimental and simulated data, hyperspectral surveys, spin state evolution of defunct GEO satellites, photometric data from Tiangong-1, and time resolution of optical light curves.

Four poster papers funded/supported by NASA ODPO were also presented over two-day sessions. James Frith presented on using the Gaia catalogue for optical observations of man-made Earth orbiting objects. Ryan Hoffman (Air Force Research Lab, AFRL) presented a joint-project review poster on optical characterization of commonly used spacecraft paints in a simulated GEO electron environment. Jacqueline Reyes (University of Texas at El Paso) focused on characterization of spacecraft materials using reflectance spectroscopy. Sue Lederer (NASA ODPO) presented a poster on integrating orbital debris measurements and modeling, as well as how observations and laboratory data are used to help make space operations safer.

There were also seven technical short courses available at the conference. Of these, two courses focused on space debris. Tim Flohrer (ESA/ESOC Space Debris Office) presented space debris risk assessment and mitigation analysis. Thomas Schildknecht (Astronomisches Institut Universität Bern) presented his course on observing and characterizing space debris.

Following the AMOS conference, the Non-Imaging Space Object Identification Workshop, hosted by Paul Kervin (AFRL) and Ryan Coder (AFRL), was held over a two-day span. Two ODPO presentations were delivered including James Frith's *"Investigations into using GAIA passbands for orbital debris material studies"* and Sue Lederer's *"Orbital Debris Characterization using UKIRT."* ♦

The 69th International Astronautical Congress (IAC), 1-5 October 2018, Bremen, Germany

More than 6000 registered participants attended the 69th International Astronautical Congress (IAC) in the "City of Space," Bremen, Germany on 1-5 October 2018. The theme of this year's IAC was "#InvolvingEveryone," which appropriately reflected the comprehensive participation from government, commercial, and academia organizations at this event organized by Team Germany. In addition to the technical programs, many plenary sessions, panel discussions, and Global Networking Forum events were offered during the week. On the last day of the IAC, Paris was selected to host the 72nd IAC in 2021.

The 16th Symposium on Space Debris held during the IAC was organized by the Space Debris Committee of the International Academy of Astronautics (IAA). This year's Symposium consisted of 10 oral presentation sessions and one interactive presentation session. The 11 sessions covered the full spectrum of space debris activities. Topics included debris detection, tracking, environment modeling, impact-induced mission effects, risk analyses and assessments, orbit determination, mitigation, and active debris removal. Two of the sessions were joint events with the Astrodynamics Symposium on "*Orbital safety and optimal operations in the increasing congested environment*" and with the Space Security Committee on "*Policy, legal, institutional and economic aspects of space debris detection, mitigation, and removal*." A total of 90 papers were presented during the oral sessions and dozens of papers were presented during the interactive session.

In addition, the IAA Space Debris Committee met to organize the 17th Space Debris Symposium for the 70th IAC (Washington, D.C.). For 2019, this year's joint session with the Astrodynamics Symposium will be replaced by a joint session with the Small Satellite Symposium to address the orbital debris aspect of large constellations and CubeSats. ♦

ABSTRACTS FROM THE NASA ORBITAL DEBRIS PROGRAM OFFICE

The 19th Advanced Maui Optical and Space Surveillance Technologies Conference, 11-14 September 2018, Maui, Hawaii, USA

The Gaia Catalogue Second Data Release and its Implications to Optical Observations of Man-made Earth Orbiting Objects

J. FRITH

The Gaia spacecraft was launched in December 2013 by the European Space Agency to produce a three-dimensional, dynamic map of objects within the Milky Way. Gaia's first year of data was released in September 2016. Common sources from the first data release have been combined with the Tycho-2 catalogue to provide a 5 parameter astrometric solution for approximately 2 million stars. The second Gaia data release is scheduled to come out in April 2018 and is expected to provide astrometry and photometry for more than 1 billion stars, a subset of which with a the full 6 parameter astrometric solution (adding radial velocity) and positional accuracy better than 0.002 arcsec (2 mas).

In addition to precise astrometry, a unique opportunity exists with the Gaia catalogue in its production of accurate, broadband photometry using the Gaia G filter. In the past, clear filters have been used by various groups to maximize likelihood of detection of dim man-made objects but these data were very difficult to calibrate. With the second release of the Gaia catalogue, a ground based system utilizing the G band filter will have access to 1.5 billion all-sky calibration sources down to an accuracy of 0.02 magnitudes or better. We discuss the advantages and practicalities of implementing the Gaia filters and catalogue into data pipelines designed for optical observations of man-made objects. ♦

Integrating Orbital Debris Measurements and Modeling – How Observations and Laboratory Data are used to Help Make Space Operations Safer

S. LEDERER, A. VAVRIN, H. COWARDIN, M. MATNEY, P. ANZ-MEADOR, AND P. HICKSON

The NASA Orbital Debris Program Office has been statistically surveying human-made resident space objects (RSOs) in geocentric orbits for several decades, using optical and infrared telescopes. The prime goal has been to understand the evolving population and characteristics of debris generated by RSOs. The debris population includes any non-functioning RSO that no longer serves a useful purpose. Any object that cannot be purposely maneuvered, including non-functioning satellites, rocket bodies, and any object generated by a collision, explosion, or fragmentation event, may pose a future collisional threat to active satellites.

Key questions immediately surface from this knowledge: What can we do to protect our precious functioning satellites from collisions? How do we design our satellites to prevent them from being future sources of debris? And what can we do as a society to protect the environment surrounding Earth to preserve it for future generations?

To begin to address these questions, and to better understand this population as well as break-up events contributing to it, NASA has developed a suite of models and experimental laboratory data to work in tandem with observational and laboratory measurements of RSOs. These models include the Orbital Debris Engineering Model (ORDEM), the Standard Satellite Break-up Model (SSBM), and an evolutionary model of the environment from LEO to GEO (LEGEND).

Ground-based data have been collected from the infrared telescope UKIRT (UK Infrared Telescope) in Hawaii, as well as the 1.3m Eugene Stansbery Meter Class Autonomous Telescope, ES-MCAT, historically called MCAT, on Ascension Island. MCAT will be tasked to collect GEO (Geosynchronous) survey data, scanning orbits to search for uncatalogued objects (*e.g.*, fragmentation/break-up events (SSBM)), and targeted observations of catalogued objects for more intensive studies, *e.g.*, when a break-up or anomalous event occurs. Laboratory experimental data includes DebriSat, a satellite impacted at ~6.9 km/s in an impact laboratory on Earth, and optical photometry from the Optical Measurements Center at NASA JSC.

An integrated view will be discussed of how our telescopic observations and lab measurements interplay with models to understand the current (ORDEM) and future (LEGEND) environment, the evolution of satellite breakups (SSBM), and how this knowledge can help to promote an environment that is safer for operations.

SHORT SUMMARY:

An integrated view will be discussed of how our telescopic observations and experimental/lab measurements interplay with models to understand the current and future environment, the evolution of satellite breakups, and how this knowledge can help to promote an environment that is safer for operations. ♦

SUBSCRIBE to the ODQN or UPDATE YOUR SUBSCRIPTION ADDRESS

If you would like to be notified when a new issue of the ODQN is published or have already subscribed but no longer receive email notifications, please update your email address using the ODQN Subscription Request Form located on the NASA Orbital Debris Program Office (ODPO) website at https://orbitaldebris.jsc.nasa.gov. You can access this form by clicking first on the "Quarterly News" tile, then selecting the navigation link within the sentence "to be notified by e-mail...".

UPCOMING MEETINGS

11-12 December 2018: The 2018 Spacecraft Anomalies and Failures Workshop, Chantilly, Virginia, USA

The 2018 Spacecraft Anomalies and Failures (SCAF) Workshop will convene 11-12 December at the James T. Mannen Conference Center in Chantilly, VA. This year's theme is "Creating a Community Solution for Anomaly Attribution," focusing on potential pathways to spacecraft anomaly attribution with special emphasis on building a "lean" anomaly attribution framework. Registration (required) is limited to US citizens and must be received by 1 December 2018. Additional information for the 2018 SCAF workshop is available at https://www.integrity-apps.com/event/scaf2018/.

26-27 February 2019: 5th Annual Space Traffic Management Conference, University of Texas at Austin – Austin, Texas, USA

The 5th Annual Space Traffic Management Conference, co-sponsored by the Spaceflight Operations Program and Applied Aviation Sciences Department of Embry-Riddle Aeronautical University's College of Aviation and the University of Texas' Strauss Center for International Security Law, has as its theme "Progress through Collaboration." Major topics of interest to the ODQN readership include space debris remediation, mitigation, and Space Situational Awareness (SSA) technologies; resident space object taxonomy and unique identification; space object and event data curation; space object information fusion; space object behavior; and spacecraft anomalies, mission assurance, and causal relationships . Abstract submission deadline for the conference passed on 8 October 2018. Additional information for the 2019 conference is available at https://commons.erau.edu/stm/2019/ .

14-19 April 2019: The 2019 Hypervelocity Impact Symposium, Destin, Florida, USA

The Hypervelocity Impact Symposium (HVIS) is a biennial event organized by the Hypervelocity Impact Society that serves as the principal forum for the discussion, interchange, and presentation of the physics of high- and hypervelocity impact and related technical areas. The HVIS Symposia have a long-standing international reputation as a catalyst for stimulating research in this area through a wealth of oral and poster presentations, and commercial exhibits. The Symposium's proceedings are the major archival source of papers published in this field. Additional information for the 2019 Symposium is available at http://www.hvis.org/symposium.htm .

15-17 May 2019: 10th International Association for the Advancement of Space Safety (IAASS) Conference, El Segundo – Los Angeles, California, USA

The 10th conference of the IAASS has as its theme "Making Safety Happen". Major debris-related topics include designing safety into space vehicles, space debris remediation, re-entry safety, nuclear safety for space missions, safety risk management and probabilistic risk assessment, and launch and in-orbit collision risk. In addition to the main sessions, four specialized sections will address Space Debris Reentries, Space Traffic Management, Safety Standards for Commercial Human Spaceflight, and Human Performance and Safety. Abstract submission deadline for the conference is 7 December 2018. Additional information for the 2019 IAASS is available at http://iaassconference2019.space-safety.org/ .

15-21 June 2019: 32nd International Symposium on Space Technology and Science, Fukui, Japan

The 32nd ISTS will be held in June 2019 in conjunction with the 9th Nano-Satellite Symposium (NSAT). This year's conference will be convened under the theme of "Fly Like a Phoenix to Space". Technical sessions include, but are not limited to, Space Environment and Debris; Space Situational Awareness; Reentry Safety; Hypervelocity Impact; Debris Risk Assessment and Management; Debris Mitigation and Removal; Space Law, Policy and International Cooperation; and Space Traffic Management. The abstract submission deadline passed on 31 October 2018. Additional information about the conference is available at http://www.ists.or.jp/index.html .

9-12 December 2019: The First International Orbital Debris Conference (IOC), Sugar Land, Texas, USA

The first of this "once-every-4-years" conference will be initiated 9-12 December 2019 in Sugar Land (near Housotn), Texas, United States. The goal of the conference is to highlight orbital debris research activities in the United States and to foster collaborations with the international community. The 4-day conference will cover all aspects of micrometeoroid and orbital debris research, mission support, and other activities. Topics to be covered include radar, optical, in situ, and laboratory measurements; engineering, long-term environment, and reentry modeling; hypervelocity impacts and protection; mitigation, remediation, policy, and environment management. The first conference announcement will be available in late 2018. See additional information at https://www.hou.usra.edu/meetings/orbitaldebris2019/ .

SATELLITE BOX SCORE

(as of 04 October 2018, cataloged by the U.S. SPACE SURVEILLANCE NETWORK)

Country/ Organization	Payloads*	Rocket Bodies & Debris	Total
CHINA	322	3665	3987
CIS	1519	5071	6590
ESA	87	57	144
FRANCE	64	491	555
INDIA	89	117	206
JAPAN	173	108	281
USA	1667	4734	6401
OTHER	895	114	1009
TOTAL	4816	14357	19173

** active and defunct*

Visit the NASA Orbital Debris Program Office Website

www.orbitaldebris.jsc.nasa.gov

Technical Editor
Phillip Anz-Meador, Ph.D.

Managing Editor
Debi Shoots

Correspondence concerning the ODQN can be sent to:

NASA Johnson Space Center
The Orbital Debris Program Office
Attn: XI5-B9E/Debi Shoots
Houston, TX 77058

debra.d.shoots@nasa.gov

National Aeronautics and Space Administration
Lyndon B. Johnson Space Center
2101 NASA Parkway
Houston, TX 77058

www.nasa.gov
https://orbitaldebris.jsc.nasa.gov/

INTERNATIONAL SPACE MISSIONS

01 July – 30 September 2018

International Designator	Payloads	Country/ Organization	Perigee Altitude (KM)	Apogee Altitude (KM)	Inclination (DEG)	Earth Orbital Rocket Bodies	Other Cataloged Debris
2018-056A	PAKTES 1A	PAKISTAN	588	625	98.0	1	6
2018-056B	PRSS 1	PAKISTAN	639	641	98.1		
2018-057A	BEIDOU IGSO-7	CHINA	35699	35879	55.0	1	0
2018-058A	PROGRESS MS-09	RUSSIA	403	408	51.6	1	0
1998-067NU	CUBERRT	USA	395	402	51.6	0	0
1998-067NV	TEMPEST-D	USA	397	405	51.6		
1998-067NW	RAINCUBE	USA	396	403	51.6		
1998-067NX	HALOSAT	USA	396	403	51.6		
1998-067NY	OBJECT NY	TBD	395	400	51.6		
1998-067NZ	OBJECT NZ	TBD	395	402	51.6		
1998-067PA	EQUISAT	USA	395	403	51.6		
1998-067PB	OBJECT PB	TBD	395	403	51.6		
1998-067PC	OBJECT PC	TBD	394	402	51.6		
2018-046C	AEROCUBE 12A	USA	477	487	51.6	0	0
2018-046D	AEROCUBE 12B	USA	477	488	51.6		
2018-046E	LEMUR 2VU	USA	477	486	51.6		
2018-046F	LEMUR 2 ALEXANDER	USA	477	486	51.6		
2018-046G	LEMUR 2TOMHENDERSON	USA	476	487	51.6		
2018-046H	LEMUR 2YUASA	USA	476	487	51.6		
2018-059A	TELSTAR 19V	CANADA	35774	35800	0.0	1	0
2018-060A	GALILEO 25 (2C1)	ESA	22971	22984	56.4	1	0
2018-060B	GALILEO 26 (2C2)	ESA	23019	23051	56.4		
2018-060C	GALILEO 23 (2C9)	ESA	23215	23229	56.4		
2018-060D	GALILEO 24 (2C0)	ESA	23086	23152	56.4		
2018-061A	IRIDIUM 160	USA	776	779	86.4	0	0
2018-061B	IRIDIUM 166	USA	776	779	86.4		
2018-061C	IRIDIUM 158	USA	776	779	86.4		
2018-061D	IRIDIUM 165	USA	776	779	86.4		
2018-061E	IRIDIUM 155	USA	776	779	86.4		
2018-061F	IRIDIUM 154	USA	776	779	86.4		
2018-061G	IRIDIUM 163	USA	776	780	86.4		
2018-061H	IRIDIUM 156	USA	776	779	86.4		
2018-061J	IRIDIUM 164	USA	776	779	86.4		
2018-061K	IRIDIUM 159	USA	776	779	86.4		
2018-062A	BEIDOU 3M9	CHINA	21510	21546	54.9	2	0
2018-062B	BEIDOU 3M10	CHINA	21515	21541	54.9		
2018-063A	GAOFEN 11	CHINA	242	648	97.4	1	0
2018-064A	TELKOM-4	INDONESIA	35782	35793	0.0	1	0
1998-067PD	OBJECT PD	TBD	397	403	51.6	0	0
1998-067PE	OBJECT PE	TBD	397	403	51.6		
1998-067PF	OBJECT PF	TBD	396	403	51.6		
2018-065A	PARKER SOLAR PROBE	USA	HELIOCENTRIC			0	0
1998-067PG	OBJECT PG	RUSSIA	399	403	51.6	0	0
1998-067PH	OBJECT PH	RUSSIA	399	404	51.6		
1998-067PJ	OBJECT PJ	RUSSIA	399	403	51.6		
1998-067PK	OBJECT PK	RUSSIA	399	403	51.6		
2018-066A	AEOLUS	ESA	307	318	96.7	0	0
2018-067A	BEIDOU 3M11	CHINA	21512	21544	55.0	2	0
2018-067B	BEIDOU 3M12	CHINA	21518	21538	55.0		
2018-068A	HAIYANG 1C	CHINA	769	787	98.6	1	0
2018-069A	TELSTAR 18V	CANADA	35781	35792	0.0	1	0
2018-070A	ICESAT-2	USA	478	482	92.0		
2018-070B	OBJECT B	USA	446	468	93.0		
2018-070C	OBJECT C	USA	446	468	93.0		
2018-070D	OBJECT D	USA	445	469	93.0		
2018-070E	OBJECT E	USA	446	468	93.0		
2018-071A	SSTL S1-4	UK	573	592	97.8	1	0
2018-071B	NOVASAR 1	UK	573	593	97.8		
1998-067PM	REMDEB-NET	UK	394	398	51.7	0	0
2018-072A	BEIDOU 3M13	CHINA	21528	21605	55.0	2	0
2018-072B	BEIDOU 3M14	CHINA	21514	21541	55.0		
2018-073A	HTV-7	JAPAN	403	408	51.6	0	0
2018-074A	AZERSPACE 2/INTELSAT 38	AZERBAIJAN	EN ROUTETO GEO			1	1
2018-074B	HORIZONS 3E	INTELSAT	35786	35787	0.1		
2018-075A	CENTISPACE-1 S1	CHINA	695	710	98.2	1	0